


## Article

# Modeling Lightning Activity in the Third Pole Region: Performance of a km-Scale ICON-CLM Simulation

Prashant Singh \* and Bodo Ahrens 

Institute for Atmospheric and Environmental Sciences, Goethe University Frankfurt, 60438 Frankfurt am Main, Germany; bodo.ahrens@iau.uni-frankfurt.de

\* Correspondence: p.singh@iau.uni-frankfurt.de

**Abstract:** The Third Pole region, especially the Himalayas, is a lightning hotspot. Predicting lightning activity in this region is difficult due to the complex monsoon and westerly circulations, as well as the complex orography. Km-scale simulations can explicitly, without parameterization, tackle deep convective phenomena. A year-long (October 2019–September 2020) ICON-CLM simulation was performed with a km-scale horizontal grid spacing of 3.3 km to assess the region’s lightning activity and evaluate the model ICON-CLM. The simulated lightning potential index (LPI) was compared against the lightning proxy  $\text{CAPE} \times \text{PREC}$  (CP) derived from ICON-CLM and reanalysis ERA5. In addition, the LPI was evaluated against the TRMM lightning climatology and observed flashes from the International Space Station Lightning Imaging Sensor (ISS-LIS). The LPI reproduced the major spatial, seasonal, and diurnal features of lightning activity as represented in the TRMM climatology. In contrast, the CP from both ICON-CLM and ERA5 performed less well regarding the location of events and the diurnal features. Taking the mean values of the LPI and CP of all the grids within  $90 \text{ km} \times 90 \text{ km}$  around the ISS-LIS detected lightning event, we found that over 80% of lightning events were recorded using the ICON-CLM simulation. Analysis of individual cases showed that the LPI predicted localization of lightning events better, but flash counts were slightly lower than the CP. Therefore, the combined use of ICON-CLM’s simulated LPI and CP can be a valuable predictor for lightning events over the Third Pole region.

**Keywords:** Tibetan Plateau; Himalayas; lightning; km-scale; ICON-CLM



**Citation:** Singh, P.; Ahrens, B.

Modeling Lightning Activity in the Third Pole Region: Performance of a km-Scale ICON-CLM Simulation.

*Atmosphere* **2023**, *14*, 1655. <https://doi.org/10.3390/atmos14111655>

Academic Editor: Farhad Rachidi

Received: 25 September 2023

Revised: 20 October 2023

Accepted: 1 November 2023

Published: 5 November 2023



**Copyright:** © 2023 by the authors. Licensee MDPI, Basel, Switzerland. This article is an open access article distributed under the terms and conditions of the Creative Commons Attribution (CC BY) license (<https://creativecommons.org/licenses/by/4.0/>).

## 1. Introduction

In comparison to other parts of the world, the Indian subcontinent has a relatively high rate of lightning-related fatalities, particularly in the Himalayan Mountains, Brahmaputra Valley, and Western Ghats [1]. Lightning and other natural disasters like cloud bursts, floods, and landslides are frequently linked to convective systems worldwide [2,3]. Over the last few decades, more than 2500 deaths per year have been reported in India as a result of direct lightning strikes, while this number was ~300 in Bangladesh and ~100 in Nepal [4–6]. Lightning fatalities are lower in developed countries such as the United States (20 per year) and less than one per million in European countries [4]. Improved predictive skills of such convective systems can help to reduce lightning related fatalities and damages. We therefore need to simulate and analyze such processes through high-resolution numerical models.

Lightning is commonly associated with thunderclouds, which are deep convective cells 5–10 km wide or wider, and 4 km deep or deeper, which can produce multiple flashes per second for 30–60 min. The presence of supercooled water, hail, and small ice crystals in the updraft process of thunderclouds produces separation of electrical charges [7,8], which may eventually result in lightning. The tropics receive the most lightning, followed by the subtropics over land [7]. Lightning prediction is still an outstanding challenge due to its random-like occurrence in space and time. Furthermore, the limited understanding of how

lightning is triggered within thunderclouds complicates prediction. With rising temperatures in a global warming scenario, the likelihood of lightning events increases [7], with some studies also suggesting an increase in intensity [8]. The study by Pérez-Invernón et al. (2023), based on convective mass flux and upward cloud–ice flux, projected a 15% global decrease in lightning activity by the end of the 21st century [9].

Traditionally, a variety of indices and parameters are used to predict thunderstorm potential, such as the K-Index (KI), lifted index (LI), total totals index (TTI), convective available potential energy (CAPE), and convective inhibition (CIN) [5,10]. In addition, earlier research has used the product of CAPE and precipitation (CP) as a reasonable indicator of lightning events [11,12]. This method takes advantage of the fact that CAPE fosters the development of convective systems, and when combined with precipitation, it becomes a reliable indicator of lightning activity. Furthermore, it is crucial to consider the various categories of lightning occurrences when forecasting the likelihood of thunderstorms. Thunderstorms can generate many forms of lightning, such as cloud-to-ground (CG), cloud-to-cloud (CC), and intra-cloud (IC) discharges [8]. Cloud-to-ground lightning is the most frequently witnessed form of lightning and presents substantial safety hazards because it has the capacity to hit the ground, resulting in wildfires and electrical disturbances [9]. In contrast, intra-cloud lightning happens exclusively within the storm cloud and does not have a direct influence on the earth's surface.

The lightning potential index (LPI) is a relatively new index developed and integrated into numerical weather models for assessing the potential of lightning activity [2]. Previous studies using various model simulations have suggested that the LPI can be used to predict lightning activity [5,10,12–15]. The LPI is calculated as the volume integral of the total mass flux of supercooled water within the developing deep convective cells; it is a derived quantity from model-simulated updraft velocities and mass mixing ratios of water, ice, snow, and graupel [2]. Since ice and graupel are the main carriers of charges within a convective cloud, the updraft speed of ice and graupel can provide a good proxy for lightning initialization. Several investigations of LPI simulations with the model Icosahedral Nonhydrostatic Climate Limited-Area Mode (ICON-CLM) and its predecessor, the COSMO-CLM, have been conducted in various regions of the world [10,16]. The ICON model's physical parameterizations are derived from the COSMO model, with additional saturation modifications for greater accuracy and performance [17,18]. Currently, no ICON-CLM-simulated LPI study is available for the complex and important Third Pole region.

In this paper, we aim to quantify to what extent the ICON-CLM model with km-scale grid spacing is capable of replicating lightning activity over the Third Pole region, utilizing the indicators LPI and CP. To reach this aim, we organized the paper into four sections. This introduction section is followed by the data and methodology section. The third section briefly discusses the lightning climatology over the Third Pole region. The fourth section of the paper examines the performance of the ICON-CLM model in predicting lightning activities. Finally, a summary and conclusion section closes the paper.

## 2. Data and Methodology

### 2.1. Lightning Observations

This study utilized two lightning observation datasets. First, the gridded lightning climatology datasets obtained from the Tropical Rainfall Measuring Mission (TRMM)—Lightning Imaging Sensor (LIS) and Optical Transient Detector (OTD) (<https://ghrc.nsstc.nasa.gov/pub/lis/climatology/LIS-OTD/>; accessed on 9 May 2023) was applied. The TRMM gridded dataset contains lightning flash counts for annual, seasonal, monthly, daily, and diurnal cycle climatology from 1995 to 2015 [13].

Second, the International Space Station (ISS)—LIS final science product (not gridded) data (ISS\_LIS\_SC\_V1.0) were used for the period of this study, October 2019–September 2020 (<https://ghrc.nsstc.nasa.gov/pub/lis/iss/data/science/final>; accessed on 9 May 2023). Following TRMM, the ISS has continued (since 2016) to record total global lightning observations, including intercloud, intra-cloud, and cloud-to-ground lightning [14]. We

used the lightning flash density index (LFDI) from the ISS-LIS. The LFDI is a spatial density metric; LFDI values are high if observed flashes are geolocated in a region of climatologically high lightning activity. Therefore, LFDI values are comparable with TRMM climatology.

The LIS from both the TRMM and ISS satellites observes the flash rate and radiant energy of lightning events at a high scale resolution during the day and night. The LIS instrument records both IC and CG discharges. This monitoring has been ongoing since the TRMM era (1995–2015) and continues to the present day with the ISS [14]. The ISS-LIS is a similar instrument to the TRMM-LIS but with increased lightning flash detection efficacy of up to 90% [14]. Since the ISS-LIS works at the wavelength 777.4 nm during daytime sunlight, reflection can cause false detection [14]. Therefore, its daytime detection efficacy is lower than nighttime detection efficacy.

The Worldwide Lightning Location Network (WWLLN) provides a good temporal and spatial coverage over the area of interest, but the WWLLN and other observational datasets are not accessible without additional costs. Therefore, the lightning flash count observations were limited to the TRMM for the lightning climatology study and the ISS-LIS for the event-based comparison.

## 2.2. Precipitation Observations

The Global Precipitation Measurement (GPM) is a multi-satellite mission that uses the integrated Multi-satellite Retrievals system (IMERG) to retrieve precipitation products [15]. We used the daily level 3 early precipitation data from the GPM-IMERG at a 0.1 degree resolution in version 6 (GPM\_3IMERGDE) for our case studies ([https://disc.gsfc.nasa.gov/datasets/GPM\\_3IMERGDE\\_06](https://disc.gsfc.nasa.gov/datasets/GPM_3IMERGDE_06); accessed on 9 May 2023).

## 2.3. Model Setup

This study used the Icosahedral Nonhydrostatic (ICON) weather and climate model in Climate Limited-Area Mode (CLM) (ICON-CLM), version 2.6.4 [16,17]. A one-year simulation period over the Third Pole region (TPR) began on 1 September 2019 and ended on 1 October 2020. A model spin-up time for the first month of simulation (September 2019) was used. The ICON-CLM simulation was performed with a km-scale (3.3 km) horizontal grid spacing with 60 vertical levels up to 10 hPa, covering the domain 22.5–42.5° N and 67.5–117.5° E. We used a smaller subdomain (25–40° N and 70–115° E, see Figure S1) for our analysis. Initial and lateral boundary conditions were provided through the ECMWF's fifth-generation atmospheric reanalysis (ERA5, available from the archive of the German Climate Computing Centre (DKRZ)) dataset [18], and the lateral boundaries were updated every hour during the simulation. For this simulation, we utilized the recently integrated and enhanced radiation scheme, ecRad [19]. Due to the very low frequency of deep convection activity over the Tibetan Plateau [20], we opted to enable Tiedtke-based shallow convection parameterization at the km-scale [21]. In addition, completely turning off/on convection parameterization at this scale can be complicated [3]. Therefore, based on previous results, we used shallow convection parameterization for this study over the Third Pole region [3,22]. A single-moment cloud microphysics scheme that predicts three ice categories, ice, snow, and graupel, was used [23] and the land surface processes were considered through the sub-model TERRA [22,24].

## 2.4. Adjusted Lightning Potential Index (LPI)

The simulated *LPI* (in J/kg) and observed lightning flashes (in counts) have different units and spatiotemporal scales; therefore, direct comparison is not possible [11]. Additionally, we used the ISS-LIS lightning flash density index observation, which was limited to two-digit numbers. To solve these problems, we first standardized the *LPI*. The standardization converted the data points to unit-less z-scores, which indicated their position relative to the mean *LPI* [25], using

$$\widehat{LPI}_{ij} = \frac{(LPI_{ij} - \overline{LPI})}{LPI_{\sigma}} \quad (1)$$

where  $\widehat{LPI}_{ij}$  is the standardized value of the  $LPI$ ,  $LPI_{ij}$  is the value of the  $LPI$  at grid point  $(i, j)$  of the domain,  $\overline{LPI}$  is the average value of the  $LPI$  over the domain, and  $LPI_{\sigma}$  is the standard deviation of the  $LPI$  over the domain. The process of standardization can have a small effect on the diurnal cycle and more likely a slight dampening of diurnal amplitudes, particularly in the regions with low  $LPI$  values.

In the second step, all the values of  $\widehat{LPI}_{ij} > 0.5$  were linearly adjusted to the observed values of lightning flashes from the ISS-LIS for each event using Equation (2). The lowest threshold of the  $LPI$  (0.5) was decided using the upper 95% percentile, to accommodate more prominent cases of lightning activity. Values below 0.5 were excluded from the calculation due to their dispersed distribution across space, posing challenges in the analysis of regions with lightning activity. In a previous study, Brisson et al. (2021) used a two-step process to adjust their parametrized output to observed flash counts using a simple linear model; they applied a threshold that any parametrized output values below 0.33 were set to 0 [11].

$$LPI_{adj} = a \times \widehat{LPI}_{ij}, \text{ for all } \widehat{LPI}_{ij} \geq 0.5 \quad (2)$$

where  $LPI_{adj}$  is the adjusted value of the  $LPI$  with  $a = 13.76$  and  $a$  obtained from a linear fit of  $LPI_{adj}$  to the ISS-LIS observed lightning flashes. The linear equation above calibrates the  $LPI$  to match the magnitude of observed flash counts without altering its diurnal cycle.

### 2.5. Product of CAPE and Precipitation (CP)

CAPE  $\times$  precipitation (CP) was used in previous studies to represent daily lightning flash rates in many regions [11,26]. For this study, we separated calculations by multiplying hourly CAPE values with hourly total precipitation from two different datasets, ICON-CLM and ERA5. Since the magnitude of the CP values was comparable to the values of observed lightning flash counts, we utilized CP in its original form. In contrast, the  $LPI$  underwent standardization and adjustments to align its magnitude with the observed values as discussed in Section 2.4.

## 3. Results and Discussion

The spaceborne long-term observation of lightning events using the TRMM provides an overview of lightning activity around the world. The monthly TRMM combined flash rate product (LISOTD\_LRMTS\_V2.3) from January 1995 to January 2015 was used to understand the yearly variation in lightning activity around the world. Figure 1 represents the time series regression coefficient (RC) of lightning activity over the TRMM coverage area. Most of the area shows a positive value of the regression coefficient, which means that over the past few years, there was an increase in lightning activity around the coverage area of the TRMM. The Western Himalayan Mountains show a higher value of the regression coefficient ( $2 \times 10^{-4}$  count/km<sup>2</sup>/day) in comparison to other parts of the world. The whole Indian subcontinent shows a positive value of the regression coefficient but is significantly lower than the Western Himalayan Mountains. The area's average lightning activity for the study domain (25°–40° N, 70°–115° E) throughout the study showed a positive value for the RC ( $5.39 \times 10^{-5}$  count/km<sup>2</sup>/day). The subdomains' (Figure S1 in Supplementary Material) analyses suggest that the trends vary from the Western Himalayan region to the Eastern Himalayan region and in the Tibetan Plateau. The Western Himalayan (WH) subdomain shows the highest increasing trend ( $6.1 \times 10^{-5}$  count/km<sup>2</sup>/day), followed by the Central Himalayan (CH) region ( $5.28 \times 10^{-5}$  count/km<sup>2</sup>/day), and the Eastern Himalayan (EH) region ( $3.08 \times 10^{-5}$  count/km<sup>2</sup>/day). However, the selected domain over the Tibetan Plateau (TP) shows no significant change in the trend ( $0.001 \times 10^{-5}$  count/km<sup>2</sup>/day).

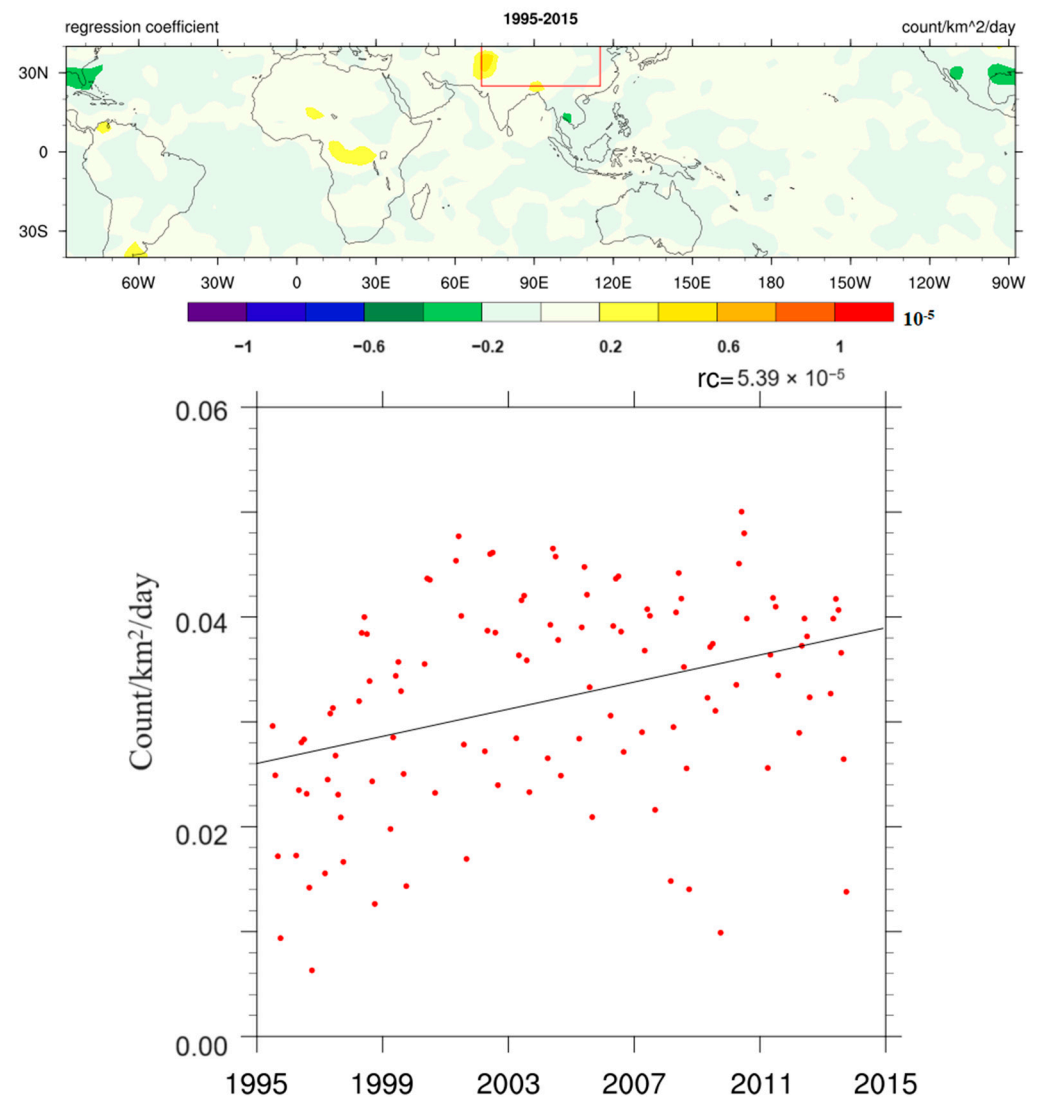


**Figure 1.** (Above) Lightning regression trend using the TRMM’s monthly product around the world and (below) time series regression over the Third Pole region (for the domain presented in the red box).

In a previous study, under the highest concentration scenario (RCP8.5), the global circulation models (GCMs) showed a substantial increase in convective available potential energy (CAPE) over the tropics and subtropics [7]. The CAPE ensemble mean from GCMs for the current climate (1981–2000) to the future climate (2081–2100) shows a  $\sim 1000$  J/kg increase over the Western Himalayan region and up to 500 J/kg over the Indo-Gangetic Plains (IGP) [7]. The increased value of CAPE indicates a greater possibility of intense and frequent lightning activity over the Western Himalayan region, like what we observed from the lightning climatology trend in Figure 1. Previous research on the Indian subcontinent has revealed a significant increase in lightning activity over the Western and Eastern Himalayan region (Figure 1), as well as the eastern coastal region of India [27], in the last two decades. The study suggested that this increasing trend of lightning activity was contributed to by changes in the surface latent heat flux (SLHF), sea surface temperature (SST), CAPE, and wind shear over the Indian subcontinent. Another long-term analysis of lightning data with respect to thermodynamic variables (CAPE, moisture, wind, etc.) along with aerosol optical depth (AOD) suggested a  $\sim 1\%$  per year increase in lightning activity over the Indian subcontinent [28]. Most of the previous studies over the Indian subcontinent have suggested an increase in the lightning trend, especially over the Western



Himalayan region and the Eastern Himalayan region (Brahmaputra Valley). As discussed in Figure 1, previous studies also showed a maximum increase rate in the Himalayan region and coastal region. This rate of increase varies over the domain depending on the availability of moisture, convection mechanisms, aerosols, etc.

The annual average values of lightning activity from the TRMM showed a significant trend using a linear regression trend test ( $p = 0.01$ ), whereas the Mann–Kendall test showed a non-significant trend ( $p = 0.07$ ). The significant increase in lightning activity over the selected domain represents a more organized and severe convective process in that region. For the very first time, a one-year-long ICON-CLM simulation at the km-scale was simulated over the HKH and the Tibetan Plateau region (TPR). The km-scale simulation can resolve deep convective processes explicitly without using convection parameterization [3,22], which can help to improve the simulation of extreme processes with greater precision compared to low-resolution simulations [29]. In recent years, the Oceanic Niño Index (ONI) for the period of October 2019 to September 2020 was within the threshold value of  $\pm 0.5$  °C. This implies less climate variability due to the El Niño–Southern Oscillation (ENSO) during the period of simulation. Previous research has indicated that lightning activity increased and decreased during El Niño and La Niña years, respectively [30–32]. A neutral ENSO period suggests a neutral effect of the ocean over the monsoon season and precipitation; therefore, for this study, we preferred to simulate October 2019 to September 2020.

As shown in Figure 2a, the TRMM climatology in the Himalayan region shows higher lightning activity compared to other regions in the domain. The Western Himalayan region shows more than 50 flashes/km<sup>2</sup>/year, followed by the Brahmaputra Valley in the Eastern Himalayan region with 50 flashes/km<sup>2</sup>/year. The southern part of the Central Himalayan region also shows significantly higher lightning activity of ~30 flashes/km<sup>2</sup>/year. Figure 2b shows the observed average lightning flashes from October 2019 to September 2020 by the ISS-LIS over the domain. For the qualitative understanding of spatial features from the ISS-LIS data, we averaged all the lightning events observed in the  $1^\circ \times 1^\circ$  grid box throughout the domain of study. The ISS-LIS also shows similar hotspots of lightning as TRMM climatology, with higher activity in the Western and Eastern Himalayan regions along with the southern part of the Central Himalayan region. Since a direct comparison was not possible due to the different units and scales of observed lightning flashes and simulated LPI [11], the adjusted LPI was used for the comparison. The adjusted LPI showed similar spatial features as observed from the ISS-LIS and the TRMM climatology. Figure 2c shows the ICON-CLM simulated time average adjusted LPI from October 2019 to September 2020 over the domain. The simulation represents similar hotspot regions in the Western Himalayan region, the Central Himalayas, and the Brahmaputra Valley. The ICON-CLM simulated significant lightning over the Central Tibetan Plateau, which is evident in climatology too, though due to scale, it was not that pronounced in Figure 2a. In previous studies, a 5-year, WLLN-based, and TRMM-based analysis showed similar spatial features of lightning activity over the study area. Those studies showed higher lightning over the Western Himalayas and foothills, followed by the Brahmaputra Valley and Tibetan Plateau [28,33,34]. Significant variation in lightning activity was reported with an elevation over the Tibetan Plateau region; the ratio of strong lightning activity was reported higher at the TP and the northern HM compared to any other region in the domain.

Figure 2d shows the average CAPE  $\times$  precipitation (CP) across the domain as derived from the ICON-CLM. The central and eastern Himalayan foothills were identified as lightning hotspots by the CP, but the Western Himalayan region, which is extremely prominent in lightning observation and climatology, is completely missing. The CP from ERA5 shows hotspots in the western and eastern parts of the domain, but these spatial features are quite far away from where the TRMM, ISS-LIS, and adjusted LPI present lightning hotspots (Figure 2e). All over the domain, the CP has values that are lower than the TRMM climatology. In the region where TRMM climatology indicates a low level of lightning activity, like the Central and Eastern TP, the adjusted LPI shows higher values

than the TRMM. However, in the region where the hotspot is located, this trend varies (Figure S2).

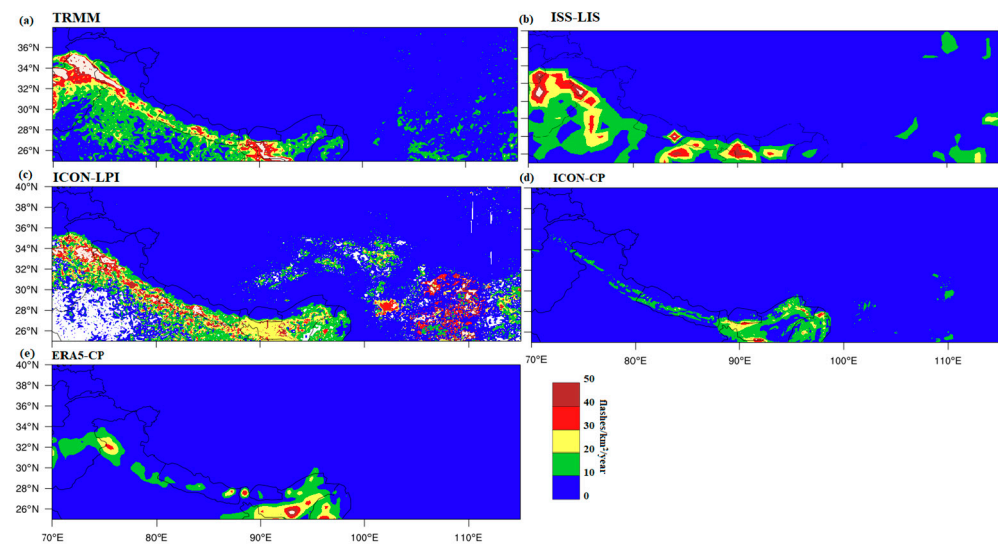


**Figure 2.** (a) Long-term (1996–2015) average of lightning flash rates from the TRMM, (b) all the events observed by the ISS-LIS during October 2019–September 2020, (c) the annual mean (October 2019–September 2020) of the adjusted lightning potential index (LPI), (d) the mean CAPE  $\times$  precipitation (CP) ICON-CLM, and (e) the CP from ERA5.

To avoid any bias due to the adjustment technique, we used the LPI and CP in their raw format for the temporal evaluation (Figure 3). In Figure 3a, the area averaged monthly means of lightning flash counts from the TRMM from 1996 to 2015 show the lowest lightning activity during the winter months of November–December–January (black dashed), whereas most of the lightning activity was observed during the June–July–August period over the Third Pole region. The ISS-LIS observed lightning activity from October 2019 to December 2020 (black) shows a similar low lightning activity period during November–December–January, but the higher activity period shows a plateau from April to August. Limited observations from the ISS-LIS and the flash count limit in the ISS-LIS might be one of the reasons for such a pattern during the monsoon season. The average value of the simulated LPI shows low lightning activity during November, December, and January (blue), which is consistent with observations and climatology. Like in climatology, the peak lightning activity period was simulated during June and July. Model simulation and observations both show a higher signature of lightning activity during the pre-monsoon months of April and May. Statistically, the monthly LPI values show a slightly higher coefficient of determination ( $r^2$ ) with the climatology of lightning activity (0.90), compared to the observed (0.72) value over the Third Pole region, where climatology and observed data show a high  $r^2$  (0.93) (sample size ( $n = 120$ )). When we examined the smaller domains, as shown in Figure S1, the LPI over the Tibetan Plateau (TP) had the highest coefficient of determination with climatology (0.96), while the Central Himalayan region had the lowest (0.81). Similar relations are observed between the LPI and observed flash counts; the TP shows a higher value of the coefficient of determination (0.94), and the Central Himalayan region shows the lowest (0.62). Unexpectedly similar coefficients of determination are present between the observations and climatology; the TP shows a higher value (0.91) and the Central Himalayan region shows the lowest (0.72) (Table S1). The significant bias in observation and simulation, as well as in observation and climatology, over the Central Himalayan region is due to a lack of satellite observation. The average value of the CP (red) shows a peak during July, whereas in other months, especially during the pre-monsoon, it shows the lowest activity, contrary to lightning climatology, observations, and the simulated LPI. The CP peak typically coincides with the seasonal convection peak over the region during July–August [35], as represented by the ERA5 CP (red dashed curve).

This indicates that the LPI represents a more realistic lightning peak during the pre- and early-monsoon periods.

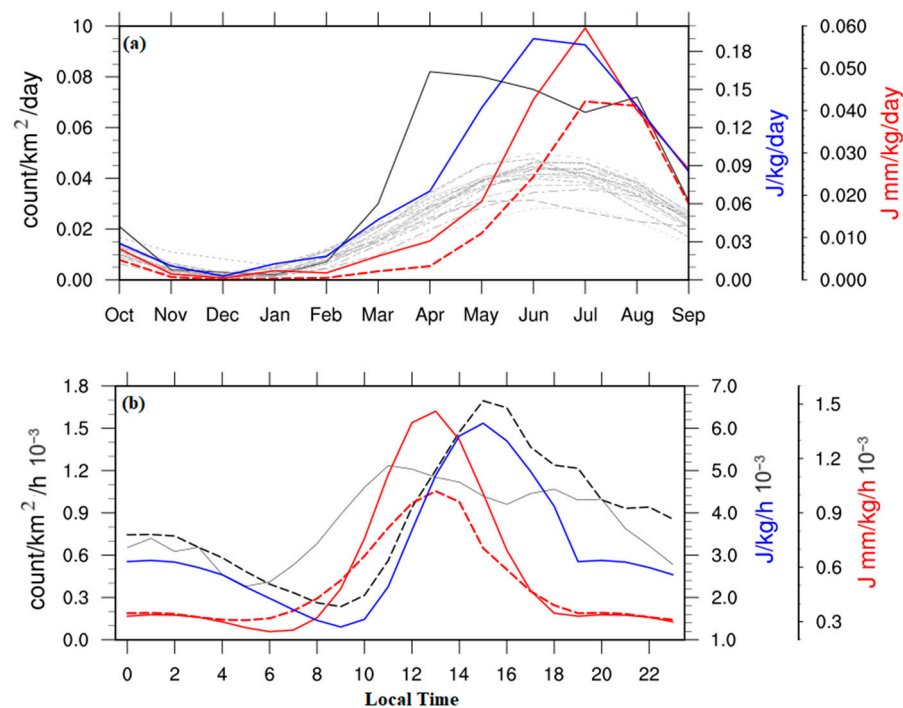


**Figure 3.** (a) Monthly occurrence of lightning over the TP region from 1995 to 2014 using the TRMM data (black dashed curve), ISS-LIS (black curve), ICON-CLM simulated LPI (blue curve) and CP (red curve), and ERA5 CP (red dashed curve) for the period of 2019–2020. (b) Average diurnal cycle using TRMM lightning climatology (black dashed curve), LIS-ISS (black curve), ICON simulated LPI (blue curve) and CP (red curve), and ERA5 CP (red dashed curve).

Further analysis of subdomains suggested different domains have peaks of lightning activity in different months. TRMM climatology suggested the TP faces maximum lightning activity in June–July [31]. The model-simulated LPI also showed a peak in June. In addition, the simulated CP and ERA5 CP showed peaks in similar months. Previous research in the TP region using WWLLN and TRMM yielded different results. The TRMM had a peak in June–July, whereas the WWLLN had a peak in August–September [36]. The authors argue this variation may be due to the WWLLN’s higher efficiency in cloud-to-ground lightning detection. Toumi and Qie (2004) discovered a June–July lightning peak using TRMM lightning data; further analyses from reanalyzed data show that pre-monsoon lightning over the TP is driven by sensible heat, whereas monsoon lightning is driven by the CAPE, and total heat flux over the region showed a similar peak as lightning activity [37]. Another study over the TP using WWLLN data showed a shift in lightning peaks from July to September as elevation increased [33]. All the previous studies have suggested a winter or post-monsoon period with the lowest lightning events over the TP, which was also replicated in the model simulation.

Lightning peaks in the western Himalayan domain occur in June–July; the LPI showed similar peaks in June–July, with a small increase in activity during the pre-monsoon period. Surprisingly, this small peak during the pre-monsoon matches an early spike presented in the CP (ICON and ERA5) during March. A few years of the lightning climatology data show this kind of pre-monsoon increase in lightning activity. The CP from both ICON and ERA5 showed a sharp peak during July–August, which coincided with the right tail of lightning climatology and the LPI curve. Previous TRMM-based studies showed a lightning peak during June–July over the WH domain [34,38]. Most research has suggested that when the northwestern monsoon transports moisture from the Arabian Sea (AS) that



meets westerlies at WH slopes, it creates a strong updraft that results in a lightning cloud over the WH region. In addition, terrain with a higher slope or higher elevation was reported to have a higher potential for lightning in the WH region [39]. Over the Central Himalayas, a peak of lightning activity was recorded during May in the TRMM lightning climatology as well as the LPI. The LPI also presented a smaller peak during July, which matched perfectly with the CP (ICON and ERA5) peak. Unlike the TP, in previous studies, TRMM-based and WLLN-based analyses over Nepal showed a similar lightning peak during May [40]. During the summer, heating of the atmosphere in the south of the CH (Terai) region amplifies atmospheric instability due to orographic lifting, resulting in deep convective events in that region [34]. Previous studies using the orographic moisture flux (OMF) and evapotranspiration showed that orographic lifting influences precipitation significantly [3,41,42]. Trapero et al. (2013) argued that the OMF values were high in a conditionally unstable environment (high CAPE) [42]. Therefore, using CP as a lightning predictor can be useful for capturing a mesoscale convection and its interaction with orography, as reflected in Figure 3a.

According to lightning climatology and the ICON-CLM LPI, the Eastern Himalayan region experiences its highest lightning activity between April and May. Higher lightning activity over the EH region during the pre-monsoon season was reported in previous studies too. Contrary to the lightning climatology of observed lightning, the CP (ICON and ERA5) showed a higher lightning peak from May to July. During the pre-monsoon season, warm air leads to convection in this region; in addition, westerlies and moisture from the Bay of Bengal provide favorable conditions for thunderclouds [34]. In the EH region, more lightning was reported in the lower area below a 500 m elevation, whereas in the WH region, higher elevations of 1000–2000 m showed high lightning [39]. Except for the Central Himalayan region, all other subdomains experience the least amount of lightning activity in December.

On average, the hourly lightning count from TRMM lightning climatology (black dashed curve) shows a peak in the afternoon over the domain of study (Figure 3b). The ISS-LIS observational data show a plateau peak structure of lightning activity that begins at early noon and lasts until late afternoon (black curve). This is because the upper observational limit of the ISS-LIS was limited to 99, resulting in a plateau structure. The simulated LPI (blue curve) shows a similar peak in the afternoon as observed in climatology. The average value of lightning flashes from the climatology over the domain of study shows a good coefficient of determination ( $n = 240$ ) with the simulated value of the LPI ( $r^2 = 0.89$ ). According to subdomain analysis, these values are quite low in the TP region (0.14) and very high in the Eastern Himalayan region (0.89). At the diurnal scale, TRMM lightning climatology had a very low  $r^2$  (0.26) with the ISS-LIS observed hourly flash count over the domain. The coefficient of determination between observation and climatology was even lower in the TP region (0.13) but significantly higher in the Central Himalayan region (0.65). The coefficient of determination for the observed flash count from the ISS-LIS was low ( $r^2 = 0.25$ ), but the coefficient of determination over the TP region was quite high (0.84) and higher in another subdomain (Table S2). The simulated CP (red curve) and ERA5 CP (red dashed curve) show a diurnal peak during the pre-afternoon period, which is earlier than the LPI and climatology peak in the region. The ICON and ERA5 CP peak in afternoon agrees with the ERA5 convective available potential energy diurnal peak [43].

Diurnal analysis from the LPI and climatology suggests a sharp afternoon peak during afternoon time over the TP region (12–4 LT); the CP from both the ICON-CLM and ERA5 shows an early peak of lightning (10–12 LT). Meanwhile, the Western Himalayas show two peaks: a higher peak during late afternoon (14–18 LT) and another lower one during early morning (00–04 LT). The CP from both the ICON and ERA5 shows two peaks over the WH region: a higher peak slightly earlier than LPI (12–14 LT) and another one that matches the LPI. Similarly, two peaks were simulated and present in climatology over the Central Himalayan region, which were less intense than in the Western Himalayas. However, over the CH region, the CP from both the ICON and ERA5 were not able to reproduce the early morning peak.

The Eastern Himalayan region showed a slightly opposite trend from the Central and Western Himalayan regions. The higher peak over the Eastern Himalayan region was in the nighttime to early morning time (22–02 LT), and another smaller peak was present during the afternoon time (12–14 LT). The CP from the ICON was able to produce a second peak over the EH region during the early morning as the LPI, but the ERA5 CP showed very low values. According to Kumar and Kumar (2021), the majority of the Himalayan region (EH, CH, and WH) has a bi-modal diurnal cycle, with a higher peak in the afternoon and a lower peak in the early morning, whereas the TP has a mono-modal diurnal pattern, with a single peak in the afternoon [34].

The TRMM lightning climatology of diurnal convection over the TP suggests a mono-modal peak during the afternoon associated with surface heating over the region [44,45]. The Indian subcontinent shows a similar convection pattern to the TP during the afternoon, with an additional peak during the evening. This justifies the observed and simulated mono-modal and bi-modal diurnal patterns over the TP and the Himalayan region, respectively. Since lightning flashes are highly correlated with surface temperature, CAPE, and moisture flux, diurnal variation is strongly dependent on the diurnal pattern of these factors. Most of the afternoon peaks correlate with high surface temperatures and CAPE, whereas the late-night peaks during the monsoon are related to moisture flux uplifted through orography over the Himalayan ranges.

When we compared lightning patterns from TRMM lightning climatology, ISS-LIS observations, and other studies, the ICON-CLM-simulated LPI did well at average spatial and temporal (seasonal and diurnal) scales. Furthermore, we wanted to look at the performance of the LPI and adjusted LPI from event-to-event observed lightning activity by the ISS-LIS from October 2019 to September 2020. The ISS-LIS observed 41,000 events, which added up to more than 3.6 million flashes during the study period, because each observed event showed LFDI values between 10 and 99. We compared the LPI at each grid point with the observations from the ISS-LIS. During the pre-monsoon period (FMAM), the model failed to produce lightning potential ( $LPI = 0$ ) for more than 73% of events at the grid level. Since lightning activity is linked to convective clouds, we tried to perform all the calculations within a certain amount of time (2 h) of the event, as suggested in the ICON-CLM evaluation [46]. At the grid level, the simulation only caught 18% of events, and 7% of the time, the model simulated a very weak signal of the LPI ( $<0.5$  J/kg). The success rate went up to 27.57%, 52.47%, and 61.26%, respectively, when the average of all the points within  $30 \times 30$  km<sup>2</sup>,  $60 \times 60$  km<sup>2</sup>, and  $90 \times 90$  km<sup>2</sup> of the point of observation was considered. From  $30 \times 30$  km<sup>2</sup> to  $90 \times 90$  km<sup>2</sup>, there was also a significant change in the weak cases: 28.56%, 17.75%, and 17.30%. During the monsoon season (JJAS), the model showed similar results at grid points but showed an increase at  $90 \times 90$  km<sup>2</sup> (Figure 4). The model-simulated LPI showed good results during the post-monsoon period (ONDJ) at the grid level, where the model was able to produce a significant LPI for 26%, and this number went up to 80% at  $90 \times 90$  km<sup>2</sup> spatial coverage. Lynn and Yair (2010) suggested that an LPI area averaged over  $36 \times 36$  km<sup>2</sup> demonstrated good results [2]. ICON-CLM simulation over the European region reported in the previous study showed an area average LPI over  $20 \times 20$  km<sup>2</sup> with good results [46]. The ICON CP performed quite better than the LPI when we considered the grid point observation of lightning events. As we considered more neighboring points around the observed event, this difference between the CP and LPI reduced significantly.

When all grids within  $90 \times 90$  km<sup>2</sup> of the observed lightning events were considered, the model produced some LPI signature events. These values varied from very low ( $<0.5$  J/kg) to two-digit numbers, but mostly they were not comparable to the observed flashes directly. On the other hand, the observed upper flash density index was also limited to 99. Due to the inconsistency of the observation data, adjusting the LPI value to observe flash counts like in the previous studies by Brisson (2021) and Schroder (2022) was not possible [11,46]. Therefore, we used the standardized value of the LPI as discussed in Equation (1) and adjusted the values of  $\widehat{LPI}$  to the observed flash count using the linear factors in Equation (2). We considered all the events up to a count of 80 flashes from the

ISS-LIS observation. In Figure 5, the warm colors (red and orange) indicate regions of higher probability density, while the cool colors (blue and green) indicate regions of low probability density. The relationship between the joint probability distribution function (PDF) of the adjusted LPI and ISS-LIS flashes for respective events is shown in Figure 5c. The greater the PDF value, the greater the likelihood of a flash count reproduced in model. The results suggest a higher coefficient of determination between the adjusted LPI and flash counts and a higher PDF ( $>0.5$ ) for the observed flash counts above 50 and the adjusted LPI below 50. While the CP values for specific events show a skewed relationship with observed flashes (Figure 5a), the TRMM lightning climatology shows a similar coefficient of determination and PDF with respect to observations (Figure 5b).

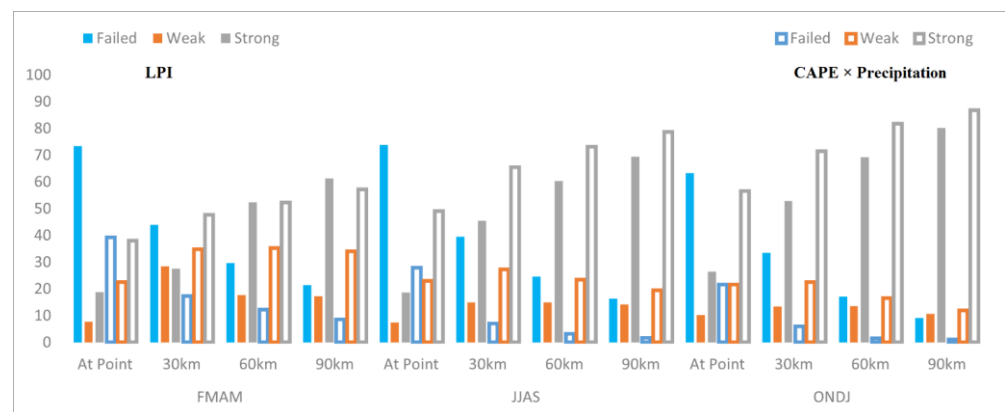


**Figure 4.** Success percentages of the ICON-CLM-simulated LPI (solid bars) and  $PR \times CAPE$  (hollow bars) vs. observed lightning activity during different seasons.

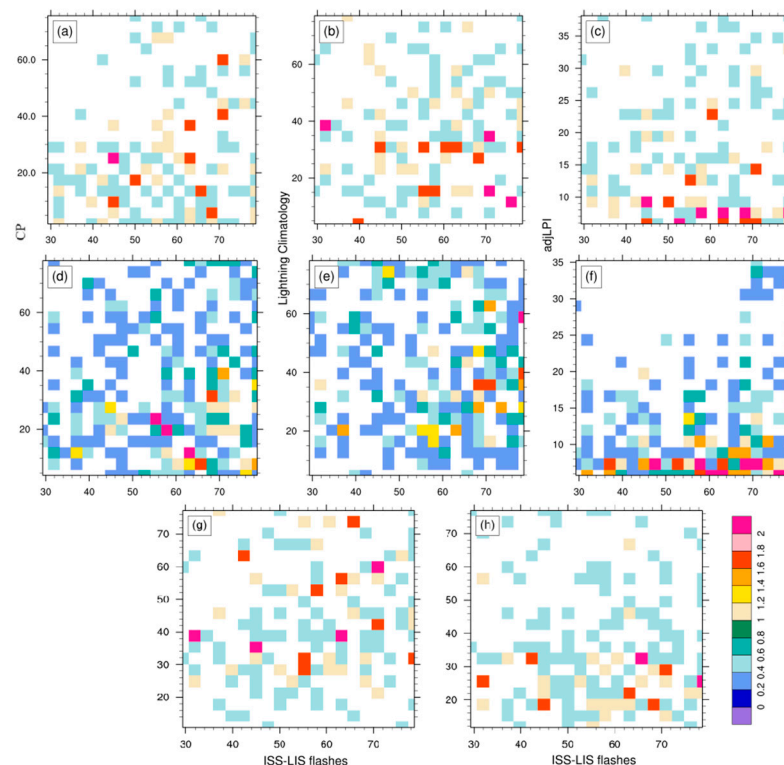


**Figure 5.** At-grid event location joint distributions of the (a) CP, (b) lightning climatology, and (c) LPIadj by ISS observation. Joint distributions of events within  $90 \times 90 \text{ km}^2$  of the observed events for the (d) CP, (e) lightning climatology, and (f) LPIadj with ISS-observed flashes. (g,h) Joint distributions for the CP, LPI, and lightning climatology with observed flashes at grid level and within  $90 \times 90 \text{ km}^2$ , respectively.

When we considered all the points within  $90 \times 90 \text{ km}^2$  of the observed event location (grid), as suggested in Figure 4, the model produced a reasonable value of the LPI. Figure 5d suggests a higher coefficient of determination between the CP and flash counts, with a higher PDF ( $>0.5$ ) for the observed flash counts above 50 and a lower value of the adjusted LPI below 30 (Figure 5f). Major events show a low coefficient of determination and a low value of the PDF for the observed events. Lightning climatology also shows a good coefficient of determination with respect to observed events (Figure 5b,e). This implies the CP performance was better in terms of flash counts compared to the adjusted LPI.

The ICON-CLM at km-scale was able to produce the signature events of lightning for most of the observed events. Grid-scale analysis concerning point of observation shows high PDF values due to the high intensity associated with the grid points (Figure 5c), whereas when we considered all the points within  $90 \times 90 \text{ km}^2$ , the detection frequency of cases increased but the PDF value decreased. Meanwhile, the CP shows a better probability distribution concerning observations (Figure 5a,d). In addition, when we considered the higher value of either the CP or LPI according to the climatology of the region for each of the observed events, the combined CP and LPI from the ICON-CLM showed a higher coefficient of determination with observed events (Figure 5g) at the grid point whereas the coefficient of determination decreased when we considered  $90 \times 90 \text{ km}^2$  around the observed events (Figure 5h). Therefore, considering the CP and LPI together for lightning prediction in the Third Pole region can be a better option than considering them separately.

When we look closely at the few chosen events out of the thousands of events that were successfully caught by simulation, we found that both the LPI and CP gave a better picture of lightning both in space and in time. Figure 6a–c show the number of lightning events and respective lightning flashes by the ISS-LIS on 22 January 2022, 3 April 2022, and 20 July 2022. Figure 6d–f show the respective values of the adjusted LPI averaged for each event within  $\pm 2 \text{ h}$ . Similarly, Figure 6g–i show CP values for the respective events. Figure 6a shows an isolated winter event; on 22 January, a single event with 38 flashes was detected by the ISS-LIS during local time ( $\sim 9 \text{ LT}$ ). The LPI at the point of observation shows a very low value, and within  $90 \times 90 \text{ km}^2$ , the average value was quite low ( $0.026 \text{ J/kg}$ ) whereas the adjusted value of the LPI showed 25 flashes when we considered the average value within  $90 \times 90 \text{ km}^2$ . Meanwhile, the CP value over the same period was quite away from the event location but in the same range (31 flashes). The event during the pre-monsoon period on 3 April (Figure 6b) shows multiple lightning events during the early morning ( $\sim 6 \text{ LT}$ ) and afternoon ( $\sim 14 \text{ LT}$ ), with flash counts ranging from 40 to 99. The adjusted LPI reproduced flash counts up to 68 (Figure 6e), and most of the event shows significant values within a  $90 \times 90 \text{ km}^2$  area. The adjusted LPI to observed flash counts (below 80) shows a high coefficient of determination ( $r^2 = 0.93$ ) whereas the CP shows a significant value (60 flash counts) concerning observed lightning events in terms of space and time. For the third case during the monsoon period on 20 July (Figure 6c), multiple lightning events (more than 400) with flash counts varying from 27 to 99 were recorded. Most of the events were recorded during the early afternoon. About 400 cases show some value of the LPI when averaged over a  $90 \times 90 \text{ km}^2$  grid of observation. The adjusted LPI shows significant comparisons for more than 200 cases. The observed lightning flashes up to 80 with an adjusted LPI show a good coefficient of determination. Many cases over the Tibetan Plateau also show a quite good value of the adjusted LPI. CP values were quite significant concerning space and time for many observed lightning events but few of the crucial observed events were captured very well with the LPI compared to the CP. The model simulated high precipitation for these events, which was complemented by satellite data too (Figure S3).

On the other hand, we analyzed, events that were completely ignored through the model-simulated lightning potential index and  $\text{CAPE} \times \text{precipitation}$  (CP). In those cases, the LPI and CP both showed no or very low values. Figure 7a–c show the number of lightning events and respective lightning flashes by the ISS-LIS on 18 January 2022, 10 April 2022, and 27 August 2022. As in the previous section, we selected one case each from the



pre-monsoon, monsoon, and post-monsoon (winter) periods. The first event on 18 January (Figure 7a) shows an isolated event during the afternoon time (~12 LT) with 31 flashes. Over the grid point as well as within  $90 \times 90 \text{ km}^2$ , the model shows zero LPI. The value of the CP (Figure 7g) shows very low values (<10 flashes) over the area of the observed lightning event; there was insignificant rain simulated through the model as well as during observations whereas the western part of the domain shows significant values of the LPI, CAPE, and precipitation. The GPM also shows significant precipitation over the western part of the domain. During the pre-monsoon period on 10 April, the ISS-LIS showed about 20 lightning events (Figure 7b), with 50 to 99 flashes during the afternoon (~13 LT). The LPI values over the region of observation were very low, along with low values of the CP, whereas the eastern part of the domain shows a high value of the adjusted LPI and CAPE. Model simulation as well as satellite data show significant precipitation in that area (Figure S4). During the monsoon on 27 August, the model showed multiple lightning events with 30 to 99 lightning events. Except for in the Western Himalayan region, the model failed to reproduce lightning activity in other parts. The Western Himalayan region during early morning time showed three events with ~40 flashes, whereas the adjusted LPI showed ~43 flashes, as well as a significantly high value of the CP. The model simulated a high amount of precipitation over the Western Himalayan region along with satellite observations, whereas other parts showed very low or negligible precipitation. It looks like the 18 January and 10 April cases were indicated as false alarms by the ISS-LIS, whereas the 27 August event over the western TP region was completely missed in the simulation.

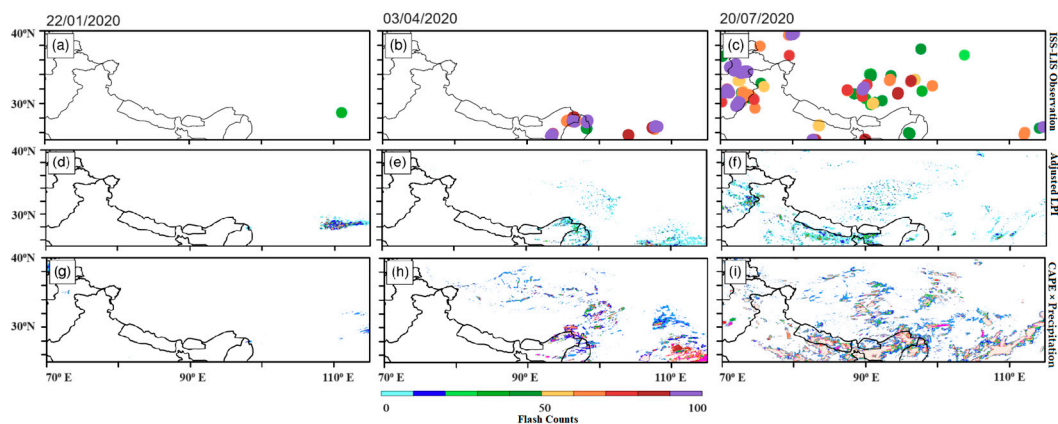


**Figure 6.** (a–c) ISS-LIS-observed lightning flash density, (d–f) adjusted LPI, and (g–i) ICON-CLM CP for the respective event dates.

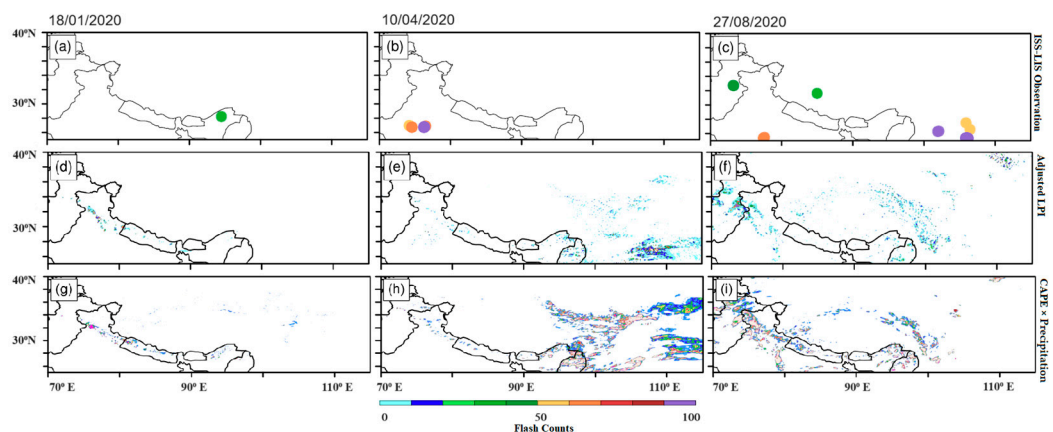


**Figure 7.** (a–c) ISS-LIS-observed lightning flash density, (d–f) adjusted LPI, and (g–i) CP for the respective event dates.



Since the LPI is calculated using the vertical motion of supercooled cloud volume and the CP is calculated using precipitation, changes in microphysics parametrization can be helpful to tune LPI and CP values over the region. Previous studies using multi-microphysical options in cloud-resolving simulations show LPI values can vary with different microphysical schemes, and the LPI along with precipitation (CP) can be helpful to predict lightning compared to the LPI alone [46,47]. Previous studies over the Bangladesh region using the WRF model showed LPI values quite off with respect to the location of observed lightning flashes in most of the cases [5]. On the other hand, ICON-CLM simulated LPIs performed quite well in terms of space and time of observed lightning activity. The CP, along with the LPI, can be a complementary validation for lightning events, but many times, the CP either fails or overpredicts the potential of lightning events. Therefore, this study suggests combining the use of the LPI and CP to capture lightning events over the Third Pole region using km-scale simulations.

#### 4. Summary and Conclusions

The spatial and temporal performance of the lightning potential index (LPI) as an indicator of lightning activity was investigated in this study, along with CAPE  $\times$  precipitation (CP). We used the LPI and CP simulated from the ICON-CLM model at a km-scale (3.3 km) resolution over the Third Pole region. The LPI from the ICON-CLM model simulation replicated spatial and temporal lightning activity features observed by the ISS-LIS and revealed in the TRMM lightning climatology. The ICON-CLM simulations indicated the Western Himalayas and the Brahmaputra Valley in the Eastern Himalayan range as lightning hotspots. Seasonal analysis showed peak lightning activity in the Western Himalayas during July caused by incoming moisture from the Arabian Sea through the northwestern monsoon branch, which gets uplifted by the westerlies and orography of the Himalayas [45,48]. In the Eastern Himalayan region, lightning peaks during the pre-monsoon month, caused by low-level atmospheric heating and incoming moisture from the Bay of Bengal. Because of the heating of the near surface and moisture from monsoon winds, the Central Himalayan and Tibetan Plateaus experience lightning peaks during monsoons.

The bi-modal diurnal cycle over the Central Himalayas and the mono-modal cycle over the Tibetan Plateau were successfully captured by the ICON-CLM simulation. The CP from the ICON-CLM and ERA5 exhibited a different seasonal and diurnal cycle than observations and the LPI, largely aligning with CAPE's diurnal and seasonal patterns. Afternoon lightning (simulated CP and LPI) peaks are mostly associated with convection due to the heating of the surface, whereas the late-night peak over the Central and Western Himalayan regions can be associated with excess moisture in the atmosphere driven by katabatic flow [49].

The ICON-CLM's adjusted LPI and CP together showed that the model can capture more than 80% of lightning events. The assessment of certain instances revealed that a modified LPI effectively recorded the occurrences, with a greater CP value in the area under scrutiny (Figures 6 and S3). In the instances where observation revealed isolated lightning, but the model was unsuccessful, the subsequent assessment indicated the absence of convective available potential energy (CAPE) and precipitation in the simulation, as evidenced by Figure 7a,b, as well as by the satellite observations depicted in Figure S4. This could be due to a misdetection of the event by the ISS-LIS. According to our analysis, we recommend combining the ICON-CLM-simulated LPI with CP over the Third Pole region for more precise lightning activity prediction, instead of using the LPI and CP independently.

**Supplementary Materials:** The following supporting information can be downloaded at: <https://www.mdpi.com/article/10.3390/atmos14111655/s1>, Figure S1: Orography of the study domains, red boxes are the area analyzed in detail; Figure S2: Annual average values of the (a) TRMM lightning climatology, (b) ISS-LIS observed data mapped on a  $1^\circ \times 1^\circ$  grid, (c) adjusted LPI, (d) difference between climatology and the adjusted LPI; Figure S3: (a–c) ICON-CLM-simulated and (d–f) observed precipitation per day for the respective events discussed in Figure 6; Figure S4: (a–c) ICON-CLM-simulated and (d–f) observed precipitation per day for the respective events discussed in Figure 7;

Table S1: Monthly regression coefficients for different domains with respect to observed lightning, climatology, and simulation; Table S2: Diurnal regression coefficients for different domains with respect to observed lightning, climatology, and simulation.

**Author Contributions:** Conceptualization, P.S. and B.A.; methodology, P.S. and B.A.; software, P.S.; validation, P.S.; formal analysis, P.S. and B.A.; investigation, P.S.; resources, B.A.; data curation, P.S.; writing—original draft preparation, P.S.; writing—review and editing, P.S. and B.A.; visualization, P.S.; supervision, B.A.; project administration, B.A.; funding acquisition, B.A. All authors have read and agreed to the published version of the manuscript.

**Funding:** This research was funded by the Deutsche Forschungsgemeinschaft (DFG, German Research Foundation)—TRR 301—Project-ID 428312742.

**Institutional Review Board Statement:** Not applicable.

**Informed Consent Statement:** Not applicable.

**Data Availability Statement:** The data presented in this study are available in the article and the supplementary material. Simulated LPI data are also available at <https://zenodo.org/records/10053518> (accessed on 9 May 2023).

**Acknowledgments:** This work was Funded by the Deutsche Forschungsgemeinschaft (DFG, German Research Foundation)—TRR 301—Project-ID 428312742. The authors would like to thank Goethe-HLR and DKRZ for providing the computational resources. We would also like to thank Danny Risto of Goethe University Frankfurt for helping in setting up the simulation. This is contribution no. 17 to CORDEX-FPS-CPTP.

**Conflicts of Interest:** The authors declare no conflict of interest.

## References

1. Albrecht, R.I.; Goodman, S.J.; Buechler, D.E.; Blakeslee, R.J.; Christian, H.J. Where are the lightning hotspots on earth? *Bull. Am. Meteorol. Soc.* **2016**, *97*, 2051–2068. [\[CrossRef\]](#)
2. Lynn, B.; Yair, Y. Prediction of lightning flash density with the WRF model. *Adv. Geosci.* **2010**, *23*, 11–16. [\[CrossRef\]](#)
3. Singh, P.; Sarawade, P.; Adhikary, B. Vertical distribution of aerosols during deep-convective event in the himalaya using WRF-chem model at convection permitting scale. *Atmosphere* **2021**, *12*, 1092. [\[CrossRef\]](#)
4. Holle, R.L. Annual rates of lightning fatalities by country. In Proceedings of the 20th International Lightning Detection Conference, Tucson, AZ, USA, 21–23 April 2008.
5. Rabbani, K.M.G.; Islam, M.J.; Fierro, A.O.; Mansell, E.R.; Paul, P. Lightning forecasting in Bangladesh based on the lightning potential index and the electric potential. *Atmos. Res.* **2022**, *267*, 105973. [\[CrossRef\]](#)
6. Sharma, S.; Neupane, B.; KC, H.B.; Koirala, M.P.; Damase, N.P.; Dhakal, S.; Gomes, C.; Cooper, M.A.; Holle, R.L.; Bhusal, R.J.; et al. Lightning threats in Nepal: Occurrence and human impacts. *Geomat. Nat. Hazards Risk* **2022**, *13*, 1–18. [\[CrossRef\]](#)
7. Singh, M.S.; Kuang, Z.; Maloney, E.D.; Hannah, W.M.; Wolding, B.O. Increasing potential for intense tropical and subtropical thunderstorms under global warming. *Proc. Natl. Acad. Sci. USA* **2017**, *114*, 11657–11662. [\[CrossRef\]](#) [\[PubMed\]](#)
8. Dieter Betz, H.; Schumann, U.; Laroche, P. Colin Price Lightning: Principles, instruments and applications: Review of modern lightning research. In *Lightning: Principles, Instruments and Applications: Review of Modern Lightning Research*; Springer Science and Business Media LLC: Dordrecht, The Netherlands, 2009; pp. 1–641. [\[CrossRef\]](#)
9. Pérez-Invernón, F.J.; Gordillo-Vázquez, F.J.; Huntrieser, H.; Jöckel, P. Variation of lightning-ignited wildfire patterns under climate change. *Nat. Commun.* **2023**, *14*, 739. [\[CrossRef\]](#)
10. Singh, P. Prediction of Potential Thunderstorm Over Ocean near Sriharikota. *Int. J. Interdiscip. Res. Innov.* **2015**, *3*, 1–6.
11. Brisson, E.; Blahak, U.; Lucas-Picher, P.; Purr, C.; Ahrens, B. Contrasting lightning projection using the lightning potential index adapted in a convection-permitting regional climate model. *Clim. Dyn.* **2021**, *57*, 2037–2051. [\[CrossRef\]](#)
12. Romps, D.M.; Charn, A.B.; Holzworth, R.H.; Lawrence, W.E.; Molinari, J.; Vollaro, D. CAPE Times P Explains Lightning Over Land But Not the Land-Ocean Contrast. *Geophys. Res. Lett.* **2018**, *45*, 12623–12630. [\[CrossRef\]](#)
13. Cecil, D.J.; Buechler, D.E.; Blakeslee, R.J. Gridded lightning climatology from TRMM-LIS and OTD: Dataset description. *Atmos. Res.* **2014**, *135–136*, 404–414. [\[CrossRef\]](#)
14. Blakeslee, R.J.; Christian, H.J.; Stewart, M.F.; Mach, D.M.; Bateman, M.; Walker, T.D.; Buechler, D.; Koshak, W.J.; O'Brien, S.; Wilson, T.; et al. Lightning imaging sensor (LIS) for the international space station (ISS): Mission description and science goals. In Proceedings of the International Conference on Atmospheric Electricity (ICAE 2014), Norman, OK, USA, 15–20 June 2014; pp. 15–20.
15. Huffman, G.J.; Gsfc, N.; Bolvin, D.T.; Braithwaite, D.; Hsu, K.; Joyce, R. *Algorithm Theoretical Basis Document (ATBD) NASA Global Precipitation Measurement (GPM) Integrated Multi-satellite Retrievals for GPM (IMERG)*; National Aeronautics and Space Administration: Washington, DC, USA, 2015; p. 29.

16. Zängl, G.; Reinert, D.; Rípodas, P.; Baldauf, M. The ICON (ICOsahedral Non-hydrostatic) modelling framework of DWD and MPI-M: Description of the non-hydrostatic dynamical core. *Q. J. R. Meteorol. Soc.* **2015**, *141*, 563–579. [\[CrossRef\]](#)
17. Van Pham, T.; Steger, C.; Rockel, B.; Keuler, K.; Kirchner, I.; Mertens, M.; Rieger, D.; Zäng, G.; Früh, B. Icon in climate limited-Area mode (icon release version 2.6.1): A new regional climate model. *Geosci. Model Dev.* **2021**, *14*, 985–1005. [\[CrossRef\]](#)
18. Hersbach, H.; Bell, B.; Berrisford, P.; Hirahara, S.; Horányi, A.; Muñoz-Sabater, J.; Nicolas, J.; Peubey, C.; Radu, R.; Schepers, D.; et al. The ERA5 global reanalysis. *Q. J. R. Meteorol. Soc.* **2020**, *146*, 1999–2049. [\[CrossRef\]](#)
19. Hogan, R.J.; Bozzo, A. ECRAD: A new radiation scheme for the IFS. *ECMWF Tech.* **2016**, *787*, 1–33.
20. Huang, J.; Zhou, X.; Wu, G.; Xu, X.; Zhao, Q.; Liu, Y.; Duan, A.; Xie, Y.; Ma, Y.; Zhao, P.; et al. Global Climate Impacts of Land-Surface and Atmospheric Processes Over the Tibetan Plateau. *Rev. Geophys.* **2023**, *61*, e2022RG000771. [\[CrossRef\]](#)
21. Tiedtke, M. A Comprehensive Mass Flux Scheme for Cumulus Parameterization in Large-Scale Models. *Mon. Weather Rev.* **1989**, *117*(8), 1779–1800. [\[CrossRef\]](#)
22. Prein, A.F.; Ban, N.; Ou, T.; Tang, J.; Sakaguchi, K.; Collier, E.; Jayanarayanan, S.; Li, L.; Sobolowski, S.; Chen, X.; et al. Towards Ensemble-Based Kilometer-Scale Climate Simulations over the Third Pole Region. *Clim. Dyn.* **2022**, *60*, 4055–4081. [\[CrossRef\]](#)
23. Doms, G.; Förstner, J.; Heise, E.; Herzog, H.-J.; Mironov, D.; Raschendorfer, M.; Reinhardt, T.; Ritter, B.; Schrodin, R.; Schulz, J.-P.; et al. *Consortium for Small-Scale Modelling a Description of the Nonhydrostatic Regional COSMO Model Part II: Physical Parameterization*; Deutscher Wetterdienst: Offenbach, Germany, 2021; Volume 6, pp. 1–152. [\[CrossRef\]](#)
24. Schulz, J.P.; Vogel, G.; Becker, C.; Kothe, S.; Rummel, U.; Ahrens, B. Evaluation of the ground heat flux simulated by a multi-layer land surface scheme using high-quality observations at grass land and bare soil. *Meteorol. Z.* **2016**, *25*, 607–620. [\[CrossRef\]](#)
25. Williams, J.W.; Jackson, S.T.; Kutzbach, J.E. Projected distributions of novel and disappearing climates by 2100 AD. *Proc. Natl. Acad. Sci. USA* **2007**, *104*, 5738–5742. [\[CrossRef\]](#)
26. Romps, D.M.; Seeley, J.T.; Vollaro, D.; Molinari, J. Projected increase in lightning strikes in the united states due to global warming. *Science* **2014**, *346*, 851–854. [\[CrossRef\]](#) [\[PubMed\]](#)
27. Qie, K.; Qie, X.; Tian, W. Increasing trend of lightning activity in the South Asia region. *Sci. Bull.* **2021**, *66*, 78–84. [\[CrossRef\]](#) [\[PubMed\]](#)
28. Chakraborty, R.; Chakraborty, A.; Basha, G.; Ratnam, M.V. Lightning occurrences and intensity over the Indian region: Long-term trends and future projections. *Atmos. Chem. Phys.* **2021**, *21*, 11161–11177. [\[CrossRef\]](#)
29. Prein, A.F.; Langhans, W.; Fossler, G.; Ferrone, A.; Ban, N.; Goergen, K.; Keller, M.; Tölle, M.; Gutjahr, O.; Feser, F.; et al. A review on regional convection-permitting climate modeling: Demonstrations, prospects, and challenges. *Rev. Geophys.* **2015**, *53*, 323–361. [\[CrossRef\]](#) [\[PubMed\]](#)
30. Yoshida, S.; Morimoto, T.; Ushio, T.; Kawasaki, Z. ENSO and convective activities in Southeast Asia and western Pacific. *Geophys. Res. Lett.* **2007**, *34*, 1–6. [\[CrossRef\]](#)
31. Ramesh Kumar, P.; Kamra, A.K. The spatiotemporal variability of lightning activity in the Himalayan foothills. *J. Geophys. Res. Atmos.* **2012**, *117*. [\[CrossRef\]](#)
32. Singh, P.; Adhikary, B.; Sarawade, P. Transport of black carbon from planetary boundary layer to free troposphere on a seasonal scale over South Asia. *Atmos. Res.* **2020**, *235*, 104761. [\[CrossRef\]](#)
33. Iwasaki, H. Relating lightning features and topography over the Tibetan Plateau using the World Wide Lightning Location Network data. *J. Meteorol. Soc. Japan* **2016**, *94*, 431–442. [\[CrossRef\]](#)
34. Kamra, A.K.; Ramesh Kumar, P. Regional variability in lightning activity over South Asia. *Int. J. Climatol.* **2021**, *41*, 625–646. [\[CrossRef\]](#)
35. Kukulies, J.; Chen, D.; Wang, M. Temporal and spatial variations of convection, clouds and precipitation over the Tibetan Plateau from recent satellite observations. Part II: Precipitation climatology derived from global precipitation measurement mission. *Int. J. Climatol.* **2020**, *40*, 4858–4875. [\[CrossRef\]](#)
36. Ma, R.; Zheng, D.; Zhang, Y.; Yao, W.; Zhang, W.; Cuomu, D. Spatiotemporal lightning activity detected by wwln over the tibetan plateau and its comparison with lis lightning. *J. Atmos. Ocean. Technol.* **2021**, *38*, 511–523. [\[CrossRef\]](#)
37. Toumi, R.; Qie, X. Seasonal variation of lightning on the Tibetan Plateau: A Spring anomaly? *Geophys. Res. Lett.* **2004**, *31*. [\[CrossRef\]](#)
38. Saha, U.; Siingh, D.; Midya, S.K.; Singh, R.P.; Singh, A.K.; Kumar, S. Spatio-temporal variability of lightning and convective activity over South/South-East Asia with an emphasis during El Niño and La Niña. *Atmos. Res.* **2017**, *197*, 150–166. [\[CrossRef\]](#)
39. Oulkar, S.; Siingh, D.; Saha, U.; Kamra, A.K. Distribution of lightning in relation to topography and vegetation cover over the dry and moist regions in the Himalayas. *J. Earth Syst. Sci.* **2019**, *128*, 180. [\[CrossRef\]](#)
40. Saha, K.; Damase, N.P.; Banik, T.; Paul, B.; Sharma, S.; De, B.K.; Guha, A. Satellite-based observation of lightning climatology over Nepal. *J. Earth Syst. Sci.* **2019**, *128*, 1–15. [\[CrossRef\]](#)
41. Hergarten, S.; Robl, J. A simple and efficient model for orographic precipitation. *Geosci. Model Dev. Discuss.* **2021**, 1–28. [\[CrossRef\]](#)
42. Trapero, L.; Bech, J.; Lorente, J. Numerical modelling of heavy precipitation events over Eastern Pyrenees: Analysis of orographic effects. *Atmos. Res.* **2013**, *123*, 368–383. [\[CrossRef\]](#)
43. Liu, Z.; Gao, Y.; Zhang, G. How well can a convection-permitting-modelling improve the simulation of summer precipitation diurnal cycle over the Tibetan Plateau? *Clim. Dyn.* **2022**, *58*, 3121–3138. [\[CrossRef\]](#)
44. Qie, X.; Wu, X.; Yuan, T.; Bian, J.; Lu, D. Comprehensive pattern of deep convective systems over the Tibetan Plateau-South Asian monsoon region based on TRMM data. *J. Clim.* **2014**, *27*, 6612–6626. [\[CrossRef\]](#)

45. Penki, R.K.; Kamra, A.K. The lightning activity associated with the dry and moist convections in the Himalayan Regions. *J. Geophys. Res. Atmos.* **2013**, *118*, 6246–6258. [[CrossRef](#)]
46. Schröder, G.; Göcke, T.; Köhler, M. Subgrid scale Lightning Potential Index for ICON with parameterized convection. *Reports ICON* **2022**, *10*, 28. [[CrossRef](#)]
47. Lagasio, M.; Parodi, A.; Procopio, R.; Rachidi, F.; Fiori, E. Lightning potential index performances in multimicrophysical cloud-resolving simulations of a back-building mesoscale convective system: The Genoa 2014 event. *J. Geophys. Res.* **2017**, *122*, 4238–4257. [[CrossRef](#)]
48. Damase, N.P.; Banik, T.; Paul, B.; Saha, K.; Sharma, S.; De, B.K.; Guha, A. Comparative study of lightning climatology and the role of meteorological parameters over the Himalayan region. *J. Atmos. Solar-Terr. Phys.* **2021**, *219*, 105527. [[CrossRef](#)]
49. Hunt, K.M.R.; Turner, A.G.; Schiemann, R.K.H. Katabatic and convective processes drive two preferred peaks in the precipitation diurnal cycle over the Central Himalaya. *Q. J. R. Meteorol. Soc.* **2022**, *148*, 1731–1751. [[CrossRef](#)]

**Disclaimer/Publisher's Note:** The statements, opinions and data contained in all publications are solely those of the individual author(s) and contributor(s) and not of MDPI and/or the editor(s). MDPI and/or the editor(s) disclaim responsibility for any injury to people or property resulting from any ideas, methods, instructions or products referred to in the content.